RSC Advances

PAPER

View Article Online
View Journal | View Issue

Cite this: *RSC Adv.*, 2026, **16**, 13669

ZrO_2-supported $LaCo_{0.5}Cu_{0.5}O_3$ composites for enhanced peroxymonosulfate activation and efficient degradation of ibuprofen

Zhaozhe Zhan,[a] Xue Yu,[ac] Jun Wan,[a] Xingchi Wang,[a] Jibo Xiao,[b] Yan Wu *[a] and Zhiyong Yan*[a]

Received 10th November 2025
Accepted 26th February 2026

DOI: 10.1039/d5ra08658b

rsc.li/rsc-advances

The tight packing of perovskite particles and secondary pollution limit their peroxymonosulfate (PMS) activation efficiency for water treatment. To address this, an eco-friendly and stable $LaCo_{0.5}Cu_{0.5}O_3$/ZrO_2 (LCCZ) catalyst is synthesized *via* a sol–gel method. Cu is introduced into the B-site of $LaCoO_3$ to form $LaCo_{0.5}Cu_{0.5}O_3$ (LaCoCu55) and then supported on ZrO_2. Characterization results confirmed the successful synthesis and dispersion of catalyst. Cu doping promoted Co^{3+}/Co^{2+} and Cu^{2+}/Cu^{+} redox cycles, while the ZrO_2 support enhanced active site exposure. Under optimized conditions (25 °C, 20 mg L^{-1} ibuprofen (IBU), 0.1 g L^{-1} LCCZ, 0.75 mM PMS, pH 7), IBU was completely degraded within 30 min. The catalyst exhibited good recyclability with minimal Co leaching (0.522 mg L^{-1}). After modification to form LCCZ, the enhanced redox cycling between Cu and Co ions, coupled with improved accessibility of active sites to PMS facilitated by the ZrO_2 support, synergistically activated PMS to generate substantial amounts of reactive species including $^1O_2$ and $^{\bullet}SO_4^-$. IBU degrades *via* $^1O_2$ and $^{\bullet}SO_4^-$-mediated oxidation, forming benzene-ring intermediates before mineralization to CO_2 and H_2O. This work guides perovskite catalyst design for IBU wastewater treatment by PMS activation.

1 Introduction

Advanced oxidation processes based on sulfate radicals ($^{\bullet}SO_4^-$) (E_0 = 2.5–3.1 eV) have been developed as more promising alternatives due to their stronger redox potentials than the hydroxyl radicals ($^{\bullet}OH$) (E_0 = 1.89–2.72 eV) that dominate traditional advanced oxidation technologies.[1] These processes possess the capability to degrade and even mineralize refractory organic pollutants.[2] Researchers typically use two oxidants, peroxymonosulfate (PMS) or peroxydisulfate (PDS), to generate $^{\bullet}SO_4^-$. However, these oxidants are relatively stable under ambient conditions and difficult to activate *via* bond cleavage for $^{\bullet}SO_4^-$ generation. Therefore, enhancing the activation efficiency of PMS or PDS has become one of the main research directions. Common activation methods include transition metal activation,[3] activated by heat,[4] ultrasonic activation[5] and UV or visible light activation.[6] Numerous transition metal oxides have been investigated as catalysts for activating PMS and PDS, such as Co_3O_4, Fe_3O_4, MnO_2, Ag_2O, *etc.* However, under acidic or neutral conditions, transition metal oxides such as Co_3O_4 and MnO_2 are prone to leaching, leading to secondary pollution. For example, although cobalt-based catalysts are highly efficient, cobalt ions are classified as potential carcinogens. Iron-based catalysts deactivate under neutral pH due to hydroxide precipitation; iron oxides like Fe_2O_3 and Fe_3O_4 exhibit drastically reduced efficiency at pH > 4, with slow Fe^{3+}/Fe^{2+} cycling and iron sludge generation. Additionally, noble metal oxides such as RuO_2 and Ag_2O incur high preparation costs.

Among them, $LaCoO_3$ perovskite exhibits favorable PMS activation capability as a transition metal oxide, its flexible chemical composition and robust structural stability have enabled widespread applications in heterogeneous advanced oxidation processes and photocatalytic systems. Compared with binary metal oxide crystals, multinary metal oxides possess more complex functions and their properties are readily adjusted by finely tuning the ratio of the component elements.[7] Furthermore, the utilization of cobalt-an earth–abundant transition metal-as the active center significantly reduces material costs compared to noble metal oxides its practical application is constrained by inherent limitations including particle agglomeration, and Co^{2+} leaching in aqueous systems-collectively restricting efficient pollutant degradation and causing secondary contamination. To overcome these challenges, developing cobalt-based lanthanum perovskites with enhanced stability, environmental compatibility, and catalytic potency has emerged as a significant research focus. Extensive studies have validated that strategic modifications *via* A-site/B-site

[a]*College of Environment and Ecology, Hunan Agricultural University, Changsha 410128, P R China. E-mail: wu_yan@hunau.edu.cn; zhyyan111@163.com*

[b]*National and Local Joint Engineering Research Center of Ecological Treatment Technology for Urban Water Pollution, Wenzhou University, Wenzhou 325035, China*

[c]*Yongji City Operation Management Limited Company, Dongguan 523000, China*

doping or composite formation can substantially enhance the catalytic functionality of perovskites.[8]

Cu substitution in $LaCo_{1-x}Cu_xO_3$ induces surface lattice oxygen migration, thereby enhancing the redox cycling efficiency between Co^{2+} and Co^{3+}. Notably, a significant deterioration in catalytic performance was observed when the substitution level reached $x \geq 0.6$. Consequently, LaCoCu55 was identified as the optimal configuration for PMS activation due to its balanced structural and electronic properties.[9] Xu *et al.*, prepared $LaCo_{1-x}M_xO_3$ (M = Cu, Fe, Mn) perovskites *via* the sol–gel method to activate peroxymonosulfate (PMS) for degrading the azo dye AO7. Among all B-site doped perovskites, Cu doping exhibited the best performance. Specifically, LaCoCu55 achieved complete AO7 removal within 20 min, whereas $LaCoO_3$ only removed 76% of AO7 in the same period.[10] This indicates that the doping of Cu ions at the B-site of $LaCoO_3$ perovskite enhances the Co^{2+}/Co^{3+} redox cycle and exhibits synergy with Co, thereby improving its catalytic performance. However, compared to pristine $LaCoO_3$, it still suffers from significant agglomeration, a low specific surface area, and Co^{2+} leaching, which limit the full utilization of its PMS activation potential.[11] ZrO_2, a p-type semiconductor metal oxide, exhibits excellent structural stability in both oxidative and reductive atmospheres. In contrast to conventional support materials like Al_2O_3 that tend to form new compounds with supported catalytic species, ZrO_2 effectively avoids such adverse reactions and consequently prevents interference with the catalytic process. Previous studies have confirmed that ZrO_2 is a more suitable support material than Al_2O_3 and SiO_2 for perovskite-catalyzed oxidation reactions.[12,13] Furthermore, compared to TiO_2, another commonly used support, although TiO_2 is one of the most studied systems because of its cheap, non-toxic and versatile physical and chemical properties,[14] ZrO_2 still demonstrates significant advantages. While TiO_2 is prone to reduction under reductive conditions or light irradiation, reductive atmosphere can significantly change the physical and chemical state of the catalyst, thus affecting its performance and stability,[15] ZrO_2 maintains high stability even under such harsh environments. Studies have also shown that ZrO_2 promotes the formation of nano-functional structures on its surface and effectively stabilizes the generated nanoparticles, suppressing their migration, agglomeration, and sintering during catalytic reactions. In summary, ZrO_2 exhibits broader application prospects compared to these conventional catalyst supports.[16] Modern catalysis traditionally focuses on optimizing the separation of active sites.[17] As a catalyst support, ZrO_2 effectively disperses perovskite particles, reduces agglomeration, and anchors metal ions to mitigate leaching. Its exceptional stability ensures durability under reactive conditions. These multifunctional characteristics collectively address the inherent limitations of LaCoCu55. Current research on metal oxide-supported modifications remai ns limited, with particularly scarce reports concerning the performance and mechanisms of perovskite-activated PMS systems for Ibuprofen (IBU) degradation.

IBU, a non-steroidal anti-inflammatory drug (NSAID), is recognized as an emerging environmental contaminant. Its persistent occurrence in aquatic systems results from high human consumption rates, low natural degradation efficiency, and limited removal by conventional wastewater treatment plants. Consequently, IBU accumulates extensively in surface waters, posing significant ecological risks through multifaceted toxicological effects—including cytotoxic and genotoxic damage and adverse impacts on growth, reproduction, and behavior of aquatic organisms, given these concerns, IBU was selected as the target pollutant in this study.

In this study, a Cu-substituted perovskite LaCoCu55 was synthesized by introducing Cu into the B-site of $LaCoO_3$, followed by the fabrication of LCCZ *via* sol–gel method. Thus, a synergistic modification strategy of "Cu doping-ZrO_2 loading" is developed, where ZrO_2 not only disperses LaCoCu55 particles but also forms a lattice-matched heterojunction to regulate the electronic structure of Co/Cu active sites and stabilize redox cycles, overcoming the trade-off between activity and stability in traditional doped perovskites. The degradation performance of IBU in different catalytic systems was systematically investigated, with emphasis on the effects of initial IBU concentration, catalyst dosage, PMS concentration, pH, reaction temperature, and common anions. Furthermore, the mechanistic pathways of IBU degradation *via* the LCCZ activated PMS system were elucidated through comprehensive analysis.

2 Experimental

2.1 Chemicals

Lanthanum nitrate hexahydrate ($La(NO_3)_3 \cdot 6H_2O$), cobalt nitrate hexahydrate ($Co(NO_3)_2 \cdot 6H_2O$), copper nitrate trihydrate ($Cu(NO_3)_2 \cdot 3H_2O$), potassium monopersulfate (PMS), and hydroxylamine hydrochloride ($NH_2OH \cdot HCl$) were purchased from Macklin Biochemical Co. Ltd (Shanghai, China). Zirconium oxide (ZrO_2), sodium bicarbonate ($NaHCO_3$), sodium dihydrogen phosphate (NaH_2PO_4), sodium chloride (NaCl), sodium nitrate ($NaNO_3$), sulfuric acid (H_2SO_4), sodium hydroxide (NaOH), p-benzoquinone ($C_6H_4O_2$), and furfuryl alcohol ($C_5H_6O_2$) (all analytical grade) were supplied by Sinopharm Chemical Reagent Co. Ltd. Methanol (CH_3OH) and *tert*-butanol ($(CH_3)_3COH$) (all chromatographic grade) were obtained from Supelco (Merck Group, Darmstadt, Germany). Citric acid monohydrate ($C_6H_8O_7 \cdot H_2O$) and ibuprofen ($C_{13}H_{18}O_2$, white powder, purity ≥98%) were acquired from Beijing Coolaber Technology Co, Ltd Ultrapure water was used throughout the experiments.

2.2 Preparation of LCCZ

The perovskite catalysts were synthesized *via* the sol–gel method.[18] LaCoCu55 nanoparticles were synthesized by weighing $La(NO_3)_3 \cdot 6H_2O$, $Co(NO_3)_2 \cdot 6H_2O$, and $Cu(NO_3)_2 \cdot 3H_2O$ in a 1 : 0.5 : 0.5 molar ratio. Each precursor was dissolved in deionized water under continuous stirring until a transparent solution formed. CA ($C_6H_8O_7 \cdot H_2O$) was then added at a metal ions-to-citric acid molar ratio of 1 : 2.5, with stirring continued until complete dissolution. The mixture was heated to 80 °C by a heat-collecting constant-temperature magnetic stirrer, and the mixture was stirred continuously for 3 hours to form

a viscous gel. The gel was transferred to a drying oven and thermally treated at 100 °C for 12 hours to eliminate residual citric acid. Subsequently, the dried precursor was calcined in a tubular furnace at 600 °C for 4 hours with a heating rate of 5 °C min^{-1}. LaCoCu55 and CA (metal ions-to-citric acid molar ratio 1 : 2.5) were dispersed in deionized water. ZrO_2 was added to the mixture according to designated loading ratios ($LaCoCu55 : ZrO_2$ = 2 : 1, 1 : 1, 1 : 2, 1 : 3). The aforementioned sol–gel procedure (gel formation, drying, and calcination) was repeated to fabricate $LaCo_{0.5}Cu_{0.5}O_3/ZrO_2$ (LCCZ) catalysts with varying loadings, designated as LCCZ-1, LCCZ-2, LCCZ-3, and LCCZ-4, respectively. The optimal loading ratio was selected through comparative experiments for subsequent use (Fig. 1).

2.3 Characterization

The morphological features of the catalysts were examined using a field-emission scanning electron microscope (FE-SEM, Carl Zeiss SIGMA 300, Germany) and transmission electron scanning microscope(TEM, JEOL JEM-F200, Japan). Crystalline structures were analyzed *via* X-ray diffraction (XRD) on a Rigaku TTRAX III diffractometer. Surface chemical states were characterized by X-ray photoelectron spectroscopy (XPS, PHI 5000C ESCA System). Specific surface areas and pore structures were determined using a Micromeritics ASAP 2460 analyzer *via* Brunauer–Emmett–Teller (BET) nitrogen adsorption–desorption measurements.

2.4 Experimental procedures and analytical methods

The IBU degradation tests were conducted in a 250 mL beaker under constant magnetic stirring at 25 °C, maintained by a temperature-controlled magnetic stirrer. A 100 mL aliquot of 20 mg L^{-1} IBU solution was transferred to the beaker, and the pH was adjusted using 0.1 mM H_2SO_4 or NaOH solutions. At reaction initiation, predetermined amounts of LCCZ catalyst and PMS were simultaneously introduced. Aliquots were periodically withdrawn, filtered through 0.22 μm membrane filters, and analyzed *via* high-performance liquid chromatography (HPLC) to quantify residual IBU concentrations.

Residual IBU concentrations were quantified by HPLC using a reversed-phase C18 column (150 mm × 4.6 mm, 5 μm) with a mobile phase of methanol and 1% phosphoric acid aqueous solution (8 : 2, v/v) at a flow rate of 0.8 mL min^{-1}, detection wavelength of 223 nm, column temperature of 35 °C, and injection volume of 10 μL. TOC analysis was performed on a Shimadzu TOC-L analyzer to monitor mineralization efficiency. Co^{2+} leaching during reactions was detected by inductively coupled plasma mass spectrometry (ICP-MS, Thermo Fisher iCAP Qc). Reactive oxygen species were identified *via* electron paramagnetic resonance (EPR) spectroscopy (JEOL FA200).Intermediate products were analyzed by liquid chromatography-mass spectrometry (LC-MS) equipped with a Welch Ultimate C18 column (2.1 × 100 mm, 3 μm), employing a mobile phase of methanol and 0.1% formic acid aqueous solution at 0.25 mL min^{-1}, with UV detection at 220 nm and 10 μL injection volume. Mass spectrometry conditions included negative electrospray ionization, a scanning range of 50–400 *m*/*z*, and molecular weight detection spanning 50–550 *m*/*z*.

3 Results and discussion

3.1 Characterization of perovskites

The morphological characteristics and distribution of LaCoCu55, ZrO_2 and LCCZ-3 were systematically characterized using field-emission scanning electron microscopy (FE-SEM) and transmission electron microscope (TEM), with results shown in Fig. 2. Analysis revealed that the LaCoCu55 perovskite exhibits a three-dimensional spherical porous foam-like structure with abundant surface voids (Fig. 2a), and the imaging demonstrated that this structure comprises irregularly shaped fine particles with significant agglomeration. In contrast, ZrO_2 displays a smooth and uniformly distributed surface morphology, providing an ideal substrate for perovskite immobilization (Fig. 2b). FE-SEM micrographs of the LCCZ-3 composite clearly demonstrate successful anchoring of

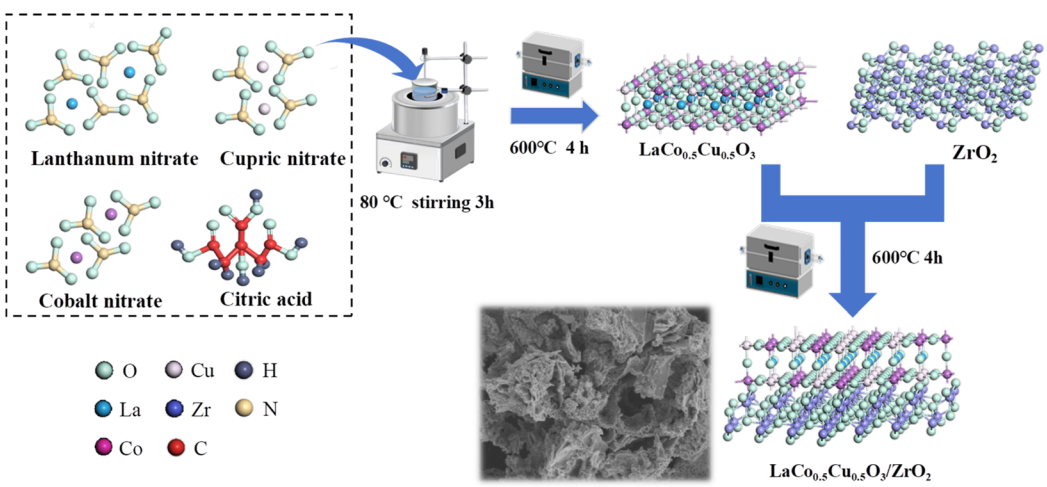

Fig. 1 Schematic illustration of the preparation process for LCCZ.

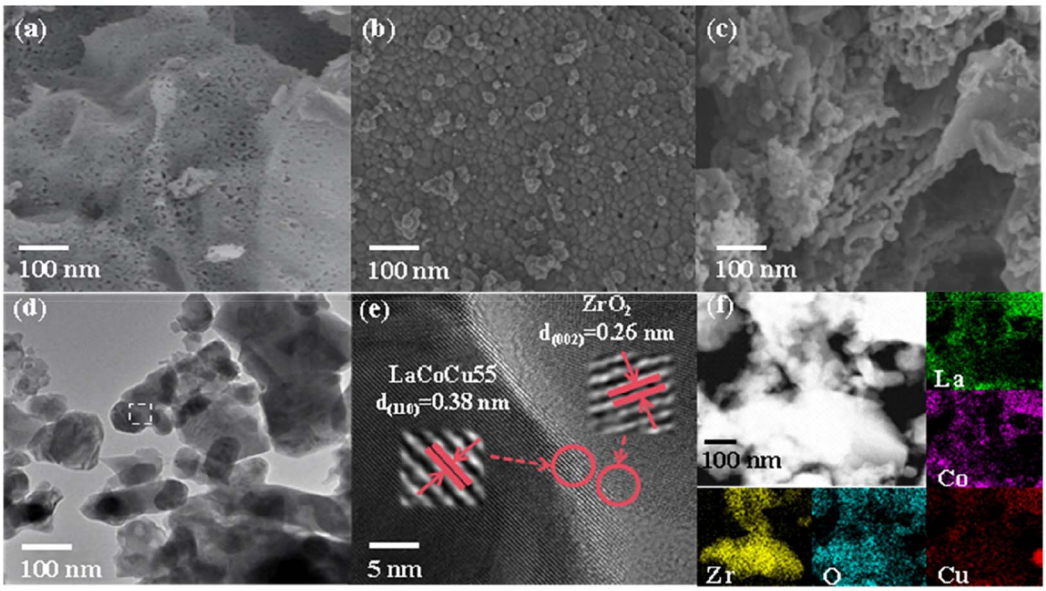

Fig. 2 SEM images of (a) LaCoCu55, (b) ZrO_2 and (c) LCCZ-3 composites, (d) TEM of LCCZ-3, (e) HRTEM of LCCZ-3, (f) elemental mapping of LCCZ-3.

LaCoCu55 onto ZrO_2.[19] When ZrO_2 serves as the support, its surface becomes fragmented and irregular, with LaCoCu55 perovskite particles embedded within the interstitial lattice sites of ZrO_2, resulting in enhanced dispersion of the perovskite phase (Fig. 2c). To further probe the interfacial relationship between LaCoCu55 and ZrO_2, TEM analysis was performed (Fig. 2d). The interface was clearly resolved in both the Fast Fourier Transform (FFT) and inverse FFT (IFFT) images. Measured lattice spacings of 0.38 nm and 0.26 nm correspond to the (110) plane of LaCoCu55 and the (002) plane of ZrO_2, respectively (Fig. 2e). Interlaced lattice fringes from these distinct phases demonstrate effective interfacial bonding between LaCoCu55 and ZrO_2. Collectively, both SEM and TEM results confirm the successful loading of LaCoCu55 onto the ZrO_2 support. EDS elemental mapping (Fig. 2f) confirmed the homogeneous distribution of La, Co, Cu, O, and Zr throughout the composite.

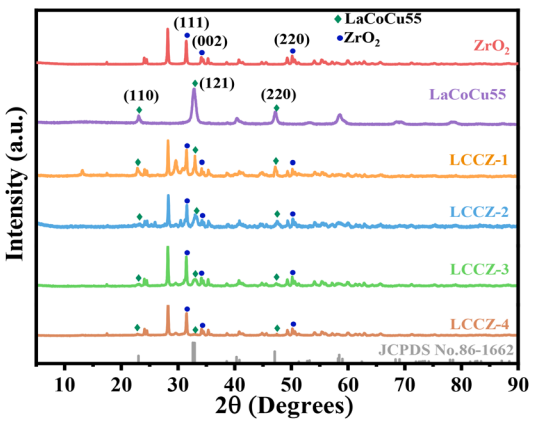

Fig. 3 XRD spectra of LaCoCu55, ZrO_2 and LCCZ-X.

The XRD patterns of LaCoCu55, ZrO_2 and LCCZ are shown in Fig. 3. LaCoCu55 exhibits characteristic diffraction peaks at 23.06°, 32.80° and 47.18°, which are assigned to the (110), (121), and (220) crystallographic planes, respectively. while ZrO_2 displays distinct peaks at 31.44°, 34.11 °and 50.12°, corresponding to the (111), (002), and (220) crystallographic planes, respectively. The XRD spectra of LCCZ incorporates all characteristic peaks from both $LaCo_{0.5}Cu_{0.5}O_3$ and ZrO_2, confirming that the synthesized catalyst retains the crystalline features of both components. This result demonstrates the successful loading of LaCoCu55 onto the ZrO_2 support. The characteristic diffraction peaks of LCCZ remained stable in all LCCZ-X samples, confirming their applicability for PMS activation. The intensities of the characteristic peaks corresponding to LaCoCu55 at 23.06°, 32.80°, and 47.18° varied with the loading amount.

The elemental composition and chemical states of the LCCZ-3 catalyst were analyzed by XPS, as illustrated in Fig. 4. The full XPS survey spectrum exhibits characteristic signals of both LaCoCu55 and ZrO_2, confirming their effective composite formation (Fig. 4a). The C 1s peak at 284.8 eV corresponds to adventitious carbon introduced during XPS calibration.[20] As observed in the La 3d spectrum (Fig. 4b), the La 3d energy level exhibits a characteristic doublet structure. The spin–orbit splitting between La $3d_{5/2}$ (834.3 eV and 837.6 eV) and La $3d_{3/2}$ (851.1 and 854.4 eV) is attributed to final-state screening effects resulting from electron correlation in the La orbitals.[21] In the Co 2p spectrum (Fig. 4c), peaks at 779.6 eV (Co^{3+} $2p_{3/2}$) and 794.7 eV (Co^{3+} $2p_{1/2}$) coexist with peaks at 781.1 eV (Co^{2+} $2p_{3/2}$) and 796.3 eV (Co^{2+} $2p_{1/2}$).[22] Similarly, the Cu 2p spectrum (Fig. 4d) shows four distinct peaks: 932.4 eV (Cu^{+} $2p_{3/2}$), 934.3 eV (Cu^{2+} $2p_{3/2}$), 952.3 eV (Cu^{+} $2p_{1/2}$) and 953.9 eV (Cu^{2+} $2p_{1/2}$).[23] The coexistence of multivalent Co and Cu facilitates redox cycling,

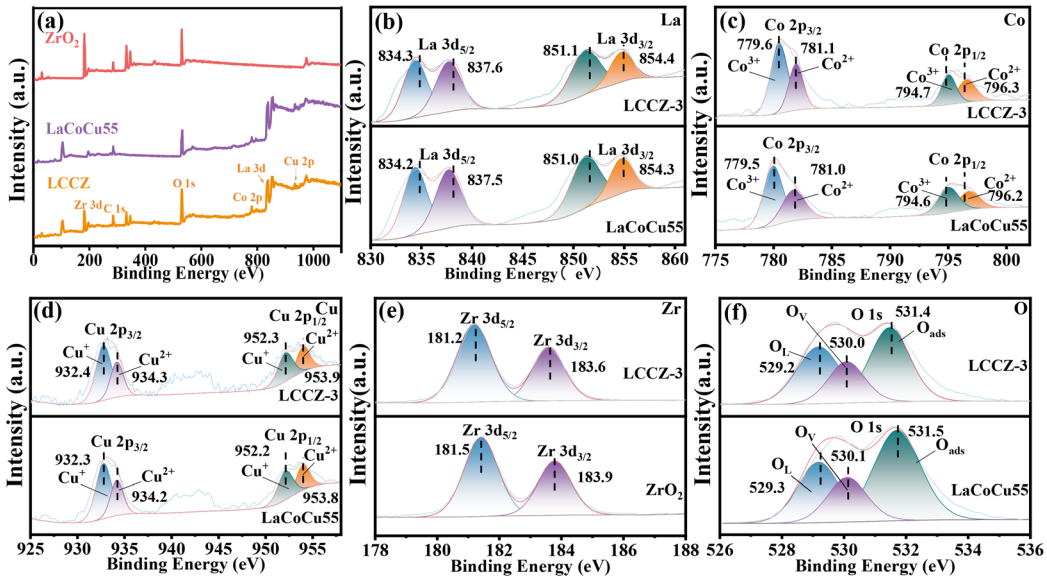

Fig. 4 Full survey XPS of (a) LaCoCu55, ZrO_2 and LCCZ, high-resolution XPS spectra of (b) La 3d, (c) Co 2p, (d) Cu 2p, (e) Zr 3d and (f) O 1s in LaCoCu55, ZrO_2 and LCCZ-3.

inducing lattice oxygen defects and promoting oxygen vacancy formation.[24] The Zr 3d high-resolution spectrum (Fig. 4e) resolves into two peaks at 181.2 eV ($3d_{5/2}$) and 183.6 eV ($3d_{3/2}$).[22] The O 1s spectrum (Fig. 4f) deconvolutes into three components: adsorbed oxygen (O_{ads},531.4 eV), oxygen vacancies (O_V, 530.0 eV), and lattice oxygen (O_L, 529.2 eV).[25] The relatively high O_{ads} content indicates a porous structure conducive to oxygen adsorption, while the presence of O_L confirms structural stability and preserved framework integrity. In the XPS analysis, evident binding energy shifts were observed after the formation of the LCCZ-3 composite. Compared with pristine LaCoCu55, the binding energies of La 3d, Co 2p, and Cu 2p in LCCZ-3 exhibited positive shifts of approximately 0.4 eV, 0.3 eV, and 0.3 eV, respectively, while the binding energies of Zr 3d and O 1s showed negative shifts of about 0.2 eV and 0.2 eV, respectively. This electronic redistribution originates from interfacial electron transfer from LaCoCu55 to the ZrO_2 support. ZrO_2 loading induces lattice distortion in the perovskite, potentially altering La–O bond lengths and angles. Such structural modifications enhance the ionic character of bonds and reduce electron density around La atoms. Concomitantly, oxygen vacancies inherently present on the ZrO_2 surface act as efficient electron-trapping centers. Electrons from reductive species within the perovskite (*e.g.*, Cu^+ or low-spin Co^{2+}) migrate to occupy these oxygen vacancies. This electron depletion oxidizes electron-donating metals (Co^{2+} and Cu^+), manifested as positive XPS shifts. Subsequent electron capture by oxygen vacancies increases electron cloud density around adjacent Zr atoms, yielding negative binding energy shifts. Neighboring O atoms also experience slight electron density increases, contributing to minor negative shifts. Quantitative XPS analysis (Table 1) indicates that the surface elemental composition of the synthesized $LaCo_{0.5}Cu_{0.5}O_3$ approximates $LaCo_{0.47}Cu_{0.46}O_{3.1}$, which exhibits a negligible deviation from the nominal stoichiometry. XPS analysis confirms the successful formation of the composite material, revealing discernible interfacial interactions between LaCoCu55 and the ZrO_2 support.

Table 1 Chemical composition of $LaCo_{0.5}Cu_{0.5}O_3$ and LCCZ-3 based on XPS data

	Atomic (%)				
Catalysts	La	Co	Cu	O	Zr
$LaCo_{0.5}Cu_{0.5}O_3$	19.88	9.43	9.12	61.57	—
LCCZ-3	12.27	4.01	3.54	69.95	10.38

The BET results are shown in Table 2. The LCCZ-3 composite exhibits a slightly lower specific surface area than pristine LaCoCu55, but with a larger average pore size. This change can be attributed to the uniform dispersion and embedding of LaCoCu55 particles within the ZrO_2 framework, which rearranges the pore structure rather than simply blocking internal voids. It should be emphasized that the improved catalytic activity of LCCZ-3 does not contradict the reduced specific surface area, because heterogeneous activation of PMS depends primarily on accessible active sites, interfacial electron transfer, and redox cycling efficiency, rather than the total specific surface area alone. As confirmed by SEM and TEM images, LaCoCu55 alone suffered from severe particle agglomeration, which caused most active Co and Cu sites to be embedded inside aggregates and thus inaccessible to PMS and IBU molecules. After loading onto ZrO_2, LaCoCu55 was highly dispersed and anchored on the support surface, which significantly increased the number of exposed and catalytically accessible active sites despite the slight decrease in total surface area.-Meanwhile, the larger pore size of LCCZ-3 reduces diffusion resistance, facilitating faster mass transport of IBU and PMS

Table 2 Specific surface area, pore volume and average pore size of LaCoCu55 and LCCZ-3

Catalysts	S_{BET} ($m^2\ g^{-1}$)	Pore volume ($cm^3\ g^{-1}$)	Pore size (nm)
LaCoCu55	22.4603	0.142286	25.7889
LCCZ-3	16.1326	0.078818	32.5281

toward active sites. XPS results further verified the formation of strong interfacial interactions and electron transfer between LaCoCu55 and ZrO_2, which stabilized the low-valence metal sites (Co^{2+}, Cu^{+}) and accelerated the Co^{2+}/Co^{3+} and Cu^{+}/Cu^{2+} redox cycles. In addition, the ZrO_2 support promoted the generation of a $^1O_2$-dominated non-radical pathway, which contributed to IBU degradation effectively and was less dependent on surface area.

3.2 Catalytic performance of the as-synthesized catalysts

Fig. 5a evaluates the degradation efficiency of IBU in eight distinct reaction systems: PMS alone, LCCZ, ZrO_2/PMS, LaCoCu55/PMS, LCCZ-1/PMS, LCCZ-2/PMS, LCCZ-3/PMS and LCCZ-4/PMS. The PMS-only system achieved only 9% IBU removal within 30 minutes, indicating that the limited oxidative capacity originated from reactive species generated through PMS self-decomposition. In the system with only LCCZ catalyst without PMS, the IBU removal rate reached 14% within 30 min, presumably due to partial adsorption of IBU by the catalyst. In the ZrO_2/PMS system, IBU removal increased to 21%, attributed to the adsorptive properties of ZrO_2. The LaCoCu55/PMS system exhibited significantly enhanced performance, achieving 76% IBU removal within 30 minutes, which underscores the effective PMS activation capability of LaCoCu55. Among the four composite systems with different loading ratios (LCCZ-1/PMS, LCCZ-2/PMS, LCCZ-3/PMS, and LCCZ-4/PMS), the LCCZ-3/PMS system demonstrated a 100% removal efficiency for IBU, which was remarkably superior to other systems. The reduced catalytic efficiency of LCCZ-1 and LCCZ-2 was attributed to the aggregation-induced decrease in active sites caused by high loading amounts, which might also block the pore channels. For LCCZ-4, the low catalytic activity was likely due to the insufficient total active sites per unit mass of catalyst resulting from the low loading amount. Thus, LCCZ-3 was selected as the optimal material for subsequent experiments.The optimized LCCZ-3/PMS system represents a more eco-friendly, stable, and highly active catalyst for actual water treatment applications compared to previously reported heterogeneous catalysts. This superiority stems from its ability to achieve complete IBU

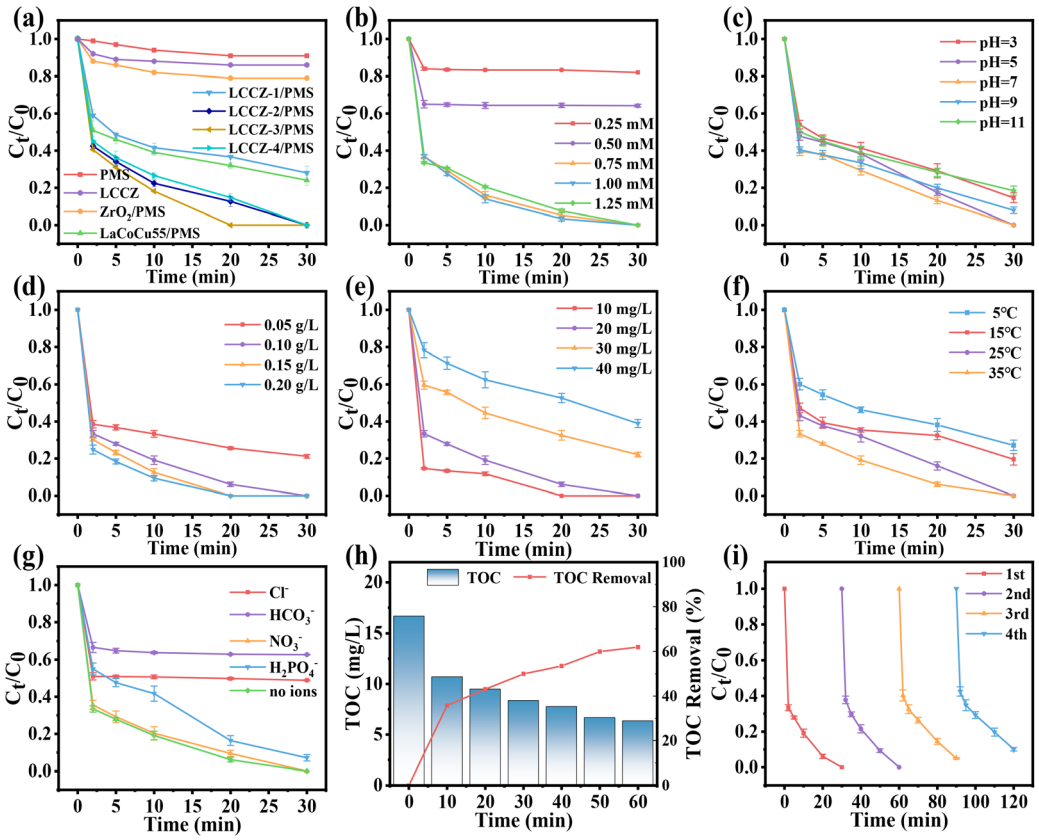

Fig. 5 (a) Degradation of IBU in various catalyst/PMS systems; effect of (b) initial PMS concentration, (c) pH of the starting solution, (d) catalyst dosage, (e) IBU concentration, (f) temperature and (g) inorganic anions on IBU removal; (h) TOC concentration variation and removal and (i) reusability of the as-synthesized catalysts. Reaction conditions: IBU = 20 mg L^{-1}, PMS = 0.75 mM, catalyst = 0.1 g L^{-1}, pH = 7, Temperature = 25 °C.

removal within a short duration while utilizing significantly lower catalyst and PMS dosages than alternative catalysts (Table 3).

PMS concentration has a significant effect on IBU removal (Fig. 5b). The IBU removal efficiency increased with PMS dosage, achieving only 16% within 30 min at 0.25 mM PMS due to insufficient oxidant availability. As the PMS concentration rose to 0.75 mM, complete IBU removal (100%) was attained within 30 min, attributable to enhanced activation of PMS generating abundant reactive species for oxidative degradation. However, further increasing PMS to 1.25 mM resulted in negligible rate enhancement and even slight reduction, likely caused by self-quenching reactions between excess PMS and reactive species.[26] To balance efficiency, cost-effectiveness, and minimized sulfate discharge, the optimal PMS concentration was determined as 0.75 mM in this study.

The effect of initial pH value on IBU removal is shown in Fig. 5c. As depicted, the optimal degradation efficiency was achieved at pH of 7. With the decrease of pH to 5, the IBU removal efficiency remained at 100%. However, a further decrease to pH of 3 resulted in a significant decline in IBU removal to 85.4%. Under strongly acidic conditions, H^+ reacts with $^{\cdot}SO_4^-$ and $^{\cdot}OH$, generating less reactive species $HSO_4^{-\cdot}$ and H_2O, thereby reducing the population of reactive radicals in the system. Conversely, as the pH increased from 7 to 11, the IBU removal efficiency continuously decreased to 81.6%. For a pH of 11, HSO_5^- dissociates into SO_5^{2-}, which diminishes the LCCZ-3 catalytic efficiency due to the weak oxidative potential of SO_5^{2-}.[27] These results indicate that both strongly acidic and strongly alkaline environments are detrimental to IBU removal within this system, although the removal efficiency remained above 80.0% under the tested conditions.

Fig. 5d demonstrates the effect of initial the catalyst dosage on degradation efficiency. LCCZ-3 acted as an activator for PMS to degrade IBU within the reaction system. The degradation rate of IBU increased markedly with increasing catalyst dosage. When the dosage of the perovskite-type catalyst was raised from 0.05 g L^{-1} to 0.2 g L^{-1}, both the removal efficiency and reaction rate exhibited significant enhancement, with the removal efficiency increasing from 79.8% to 100%. This improvement is primarily attributed to the increased number of active sites provided by the higher catalyst dosage, which accelerated the activation of PMS. However, the rate of increase in reaction rate diminished with further increments in catalyst dosage. This phenomenon is mainly due to the self-quenching of a portion of the radicals generated during the initial stage of PMS activation at higher catalyst loadings, where excessive radical concentrations were produced. To achieve a cost-effective operation, the optimal catalyst dosage in this study was determined to be 0.1 g L^{-1}.

The degradation efficiency of IBU was greatly affected by the initial IBU concentration (Fig. 5e). As shown, an increase in the initial IBU concentration resulted in a decrease in the IBU removal efficiency. Specifically, when the initial IBU concentration was raised from 10 mg L^{-1} to 40 mg L^{-1}, the removal efficiency declined from 100% to 61.1%. This reduction in removal efficiency can be attributed to the higher initial IBU concentration requiring a greater quantity of reactive radicals for its degradation. Concurrently, the amount of intermediate products generated during the degradation process increased correspondingly. These intermediates compete with IBU for the available reactive radicals, thereby diminishing the overall IBU removal efficiency.

Temperature variation indirectly influences the system's efficacy by altering the collision frequency between reactive species and pollutant molecules through its effect on molecular motion within the solution. As the temperature increased, the IBU removal efficiency rose from 72.9% to 100%, indicating enhanced degradation performance at higher temperatures (Fig. 5f). Generally, elevated temperatures promote both the adsorption of ibuprofen (IBU) and electron transfer processes, thereby generating a greater quantity of reactive species and accelerating the reaction rate. Nevertheless, the removal efficiency still exceeded 80% even under lower temperature conditions.

Various inorganic anions are ubiquitous in real aquatic environments, which might affect the PMS activation in wastewater treatment as well. Therefore, the effect of various anions relevant in aqueous systems (such as Cl^-, NO_3^-, $H_2PO_4^-$, HCO_3^-, *etc.*) on the IBU removal with LCCZ-3 was analyzed (Fig. 5g). The presence of Cl^-, NO_3^-, $H_2PO_4^-$, and HCO_3^- exhibited varying inhibitory effects on the catalytic

Table 3 Comparison of the IBU removal by LCCZ-3 with those other catalysts in the literature

Catalysts	Dosage (g L^{-1})	IBU conc (mg L^{-1})	PMS conc (mmol L^{-1})	Time (min)	IBU removal (%)	References
LCCZ-3	0.1	20	0.75	30	100	This work
Co_3O_4-rGO	0.1	30	2	30	94.5	33
B-CuO	0.1	4	0.6	30	92.9	34
Co_{SA}-N-$C_{O,S}$	0.2	10	2	10	98.2	35
C-ZnFe LDH	1	5	1	90	74.5	36
Fe_3C/NC	0.1	10	3.3	30	95	37
H_3BO_3–CuO	0.1	4	0.6	30	98.3	38
Co/D001	0.3	10	0.7	60	70	39
γFe_2O_3@$Ti_3C_2T_x$	0.2	20	0.33	90	95.7	40
Co/Fe@CNFs	0.2	5.2	10	60	100	41
SACs Cu@C	0.1	10	0.16	30	91.3	42

reaction.Cl^- preferentially reacts with $^{\bullet}SO_4^-$, generating less reactive chlorine radicals ($^{\bullet}Cl$), thereby attenuating IBU degradation. HCO_3^-significantly suppressed PMS decomposition through competitive adsorption on catalytic active sites, impeding electron transfer processes. Additionally, HCO_3^- scavenges $^{\bullet}SO_4^-$ and $^{\bullet}OH$ to form weakly oxidizing species.[28,29] NO_3^- caused mild inhibition without altering solution pH or PMS stability.[30] $H_2PO_4^-$ adversely affected the system by: (i) modifying solution pH, destabilizing PMS and altering catalyst surface charge; and (ii) strongly complexing with active metal sites on the catalyst surface, blocking reactive centers. The inhibition hierarchy followed: $HCO_3^- > Cl^- > H_2PO_4^- > NO_3^-$, highlighting the critical impact of anion chemistry on advanced oxidation performance in complex aqueous matrices.[31,32]

To evaluate the mineralization capability of the LCCZ-3/PMS system, TOC analysis was conducted before and after the reaction. The TOC decreased from 16.7 mg L^{-1} to 6.34 mg L^{-1} after 60 min, achieving a mineralization efficiency of 61.94% (Fig. 5h). This significant reduction in organic carbon content demonstrates the system's exceptional mineralization capability for converting ibuprofen into inorganic end-products.

The reusability of the PMS-activating material is crucial for practical applications. To evaluate the recyclability of the catalyst, the material was recovered after each reaction cycle *via* centrifugation, washed, dried, and subsequently reused for degradation experiments, with a total of 4 cycles performed. The results demonstrate that the stability and PMS activation efficiency of LCCZ-3 remained largely unaffected during the first three cycles (Fig. 5i). However, in the 4th cycle, a decrease in the reaction rate for IBU removal was observed, and complete degradation of IBU was not achieved, with the degradation efficiency dropping to 92.9%. This decline is likely attributable to the accumulation of residual IBU and its intermediate products on the catalyst surface after multiple uses, reducing the number of available active sites for PMS activation and consequently impairing the reaction kinetics.[43] Furthermore, ICP-MS analysis of the post-reaction solution revealed Co ions concentration of 0.522 mg L^{-1}, indicating that leaching of catalytically active Co ions also contributes to the diminished catalytic activity. This value is below or close to the industrial discharge limits for cobalt specified in many national and international regulations, such as the Chinese standard GB 25467-2010 (indirect discharge: $\leq$1.0 mg L^{-1}). Although Co ion leaching can adversely affect catalyst reusability, the exceptionally low leaching level (0.522 mg L^{-1} from a 0.1 g L^{-1} catalyst dosage) demonstrates the outstanding stability and excellent recyclability of this material, effectively mitigating concerns about secondary Co contamination.

To investigate the post-reaction stability of the material, XPS was employed to analyze the elemental composition and chemical states. The XPS survey spectrum (Fig. 6a) revealed that the characteristic peaks of LCCZ-3 remained consistent before and after the reaction, indicating retention of the original chemical states. However, the relative contents of the transition metal elements changed due to the reaction. As shown in Fig. 6b, the relative proportions of Co^{2+} and Co^{3+} were 39.6% and 60.4% before the reaction, shifting to 41.2% and 58.8% after the reaction. Similarly, Fig. 6c shows the relative proportions of Cu^+ and Cu^{2+} changed from 44.7% and 55.3% before the reaction to 54.3% and 45.7% afterward. This corresponds to increases of 1.6% for Co^{2+} and 9.6% for Cu^+ in their respective elemental abundances. These changes demonstrate the crucial roles of both transition metals in the catalytic performance. The preserved catalytic activity after reaction is attributed to the sustained redox cycling between Co^{3+}/Co^{2+} and Cu^{2+}/Cu^+ pairs. Furthermore, the relative proportions of lattice oxygen (O_L) and oxygen vacancies (O_V) decreased from 35.5% and 21.5% to 29.4% and 20.5%, respectively, post-reaction, likely due to their participation in the redox processes (Fig. 6d). Collectively, these XPS results confirm the excellent stability and reusability of the LCCZ-3 catalyst.

3.3 Identification of the major active species

To elucidate the catalytic mechanism of IBU degradation in the LCCZ-3/PMS system, quenching experiments were performed to identify the primary reactive species responsible for IBU degradation. Methanol (MeOH) effectively scavenges both $^{\bullet}SO_4^-$ and $^{\bullet}OH$, while tert-butanol (TBA) reacts significantly slower with $^{\bullet}SO_4^-$ than with $^{\bullet}OH$, making TBA a relatively selective scavenger for $^{\bullet}OH$. p-BQ was used to quench $^{\bullet}O_2^-$,[44] and furfuryl alcohol (FFA) was employed as a scavenger for $^1O_2$.[45]

The addition of a high concentration of MeOH (0.50 M) significantly suppressed IBU removal to 8.7% within 30 minutes of reaction. In contrast, adding 0.50 M TBA resulted in a less pronounced inhibition, with the IBU removal efficiency decreasing to 53.7% (Fig. 7a). This demonstrates that MeOH exerted a much stronger inhibitory effect than TBA. These results indicate the coexistence of both $^{\bullet}SO_4^-$ and $^{\bullet}OH$ within the reaction system, with $^{\bullet}SO_4^-$ playing the dominant role in the oxidative degradation and $^{\bullet}OH$ acting in a secondary capacity. Due to potential interference with IBU measurement at high concentrations, lower concentrations of p-BQ and FFA were selected to probe the presence of $^{\bullet}O_2^-$ and $^1O_2$. The addition of 0.50 mM FFA exhibited a similarly strong inhibitory effect as MeOH, reducing IBU removal to 5.9%. When 0.50 mM p-BQ was added, the IBU removal efficiency was 21.4%. This suggests that a minor contribution from $^{\bullet}O_2^-$ may exist within the system. It should be noted that p-BQ can also scavenge $^{\bullet}OH$ at neutral pH, implying that $^{\bullet}O_2^-$ likely participates in the catalytic reaction. Furthermore, $^{\bullet}O_2^-$ can interact with water molecules to generate $^1O_2$. The most significant inhibition was observed with FFA, indicating that $^1O_2$ is also a major reactive species in this system.

Building upon the preliminary identification of reactive species ($^1O_2$, $^{\bullet}SO_4^-$, $^{\bullet}O_2^-$, and $^{\bullet}OH$) in the LCCZ-3/PMS system through quenching experiments, EPR spectroscopy was employed to definitively identify the specific reactive species. Characteristic signals for both the DMPO-$^{\bullet}OH$ adduct (with hyperfine splitting constants $\alpha H = \alpha N = 14.8$ G) and the DMPO-$^{\bullet}SO_4^-$ adduct ($\alpha N = 13.2$ G,$\alpha N = 9.6$ G, $\alpha H = 1.48$ G, $\alpha H = 0.78$ G) were observed upon adding $LaCo_{0.5}Cu_{0.5}O_3/ZrO_2$ to PMS (Fig. 7b). This confirms the concurrent generation of both $^{\bullet}OH$

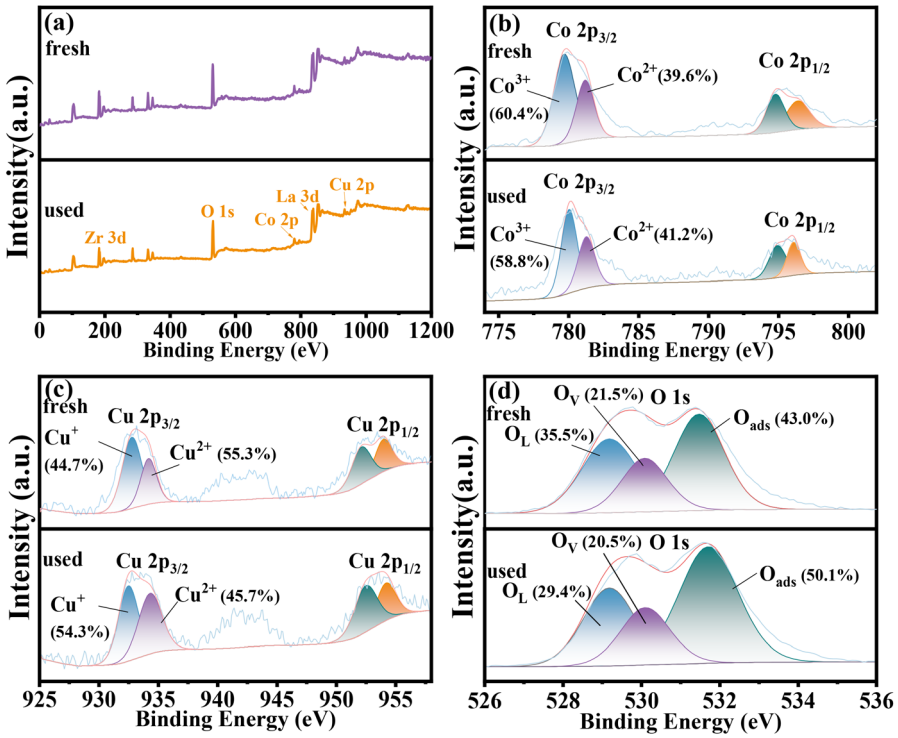

Fig. 6 Full survey XPS of (a) LCCZ-3, high-resolution XPS spectra of (b) Co 2p, (c) Cu 2p and (d) O 1s of LCCZ-3 before and after the reaction.

and $^{\bullet}SO_4^-$ radicals within the reaction system.[46] Furthermore, The characteristic 1 : 1 : 1 triplet signal of the TEMP-$^1O_2$ adduct ($\alpha N = 1.72$ mT) when TEMP was added, unequivocally demonstrating the involvement of $^1O_2$ in the catalytic process (Fig. 7c), likely attributable to the presence of oxygen vacancies in the catalyst material.[47] Fig. 7d presents a six-line spectrum

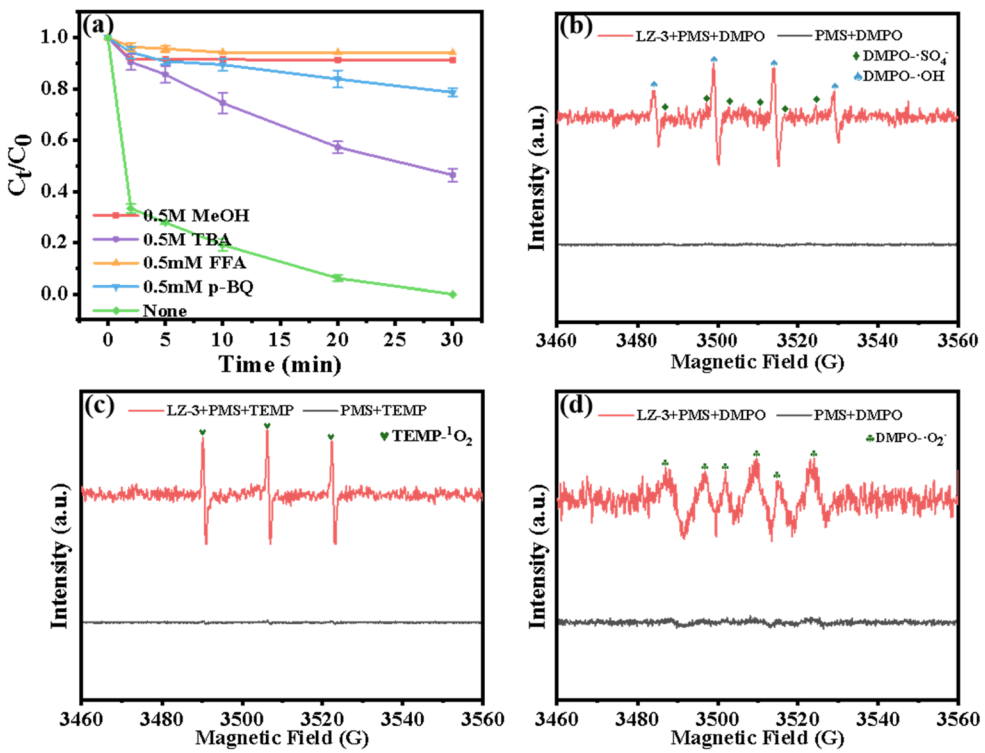

Fig. 7 (a) Experiment with quenching; ESR detection (b) $^{\bullet}OH$ and $^{\bullet}SO_4^-$, (c) $^1O_2$, (d) $^{\bullet}O_2^-$.

with a 1 : 1 : 1 : 1 : 1 : 1 intensity ratio and pairwise adjacent peaks, providing evidence for the formation of $^{\cdot}O_2^-$.

3.4 Catalytic mechanism

The catalytic mechanism of IBU degradation in the LCCZ-3/PMS system involves both radical and non-radical oxidation pathways (Fig. 8). For the radical pathway, $^{\cdot}SO_4^-$ are generated through the reaction between PMS and surface Co^{2+} sites (eqn (1)), nd part of $^{\cdot}SO_4^-$ can be further converted into hydroxyl radicals (eqn (2)).[48] Meanwhile, the standard reduction potential of Co^{3+}/Co^{2+} (1.81 V) significantly exceeds that of Cu^{2+}/Cu^{+} (0.17 V), facilitating rapid Cu^{+}-mediated reduction of Co^{3+} to Co^{2+} (eqn (3)), thereby enhancing perovskite activity. Furthermore, Cu^{2+} reacts with PMS to produce Cu^{+} and $^{\cdot}SO_5^-$ with weak activity (eqn (4)).

Regarding non-radical routes, HSO_5^- produces e^- by deprotonation (eqn (5)), and electrons can react with oxygen to produce $^{\cdot}O_2^-$ (eqn (6)). $^1O_2$, as the dominant non-radical species, is mainly produced by the reaction of oxygen vacancies or surface lattice oxygen with PMS (eqn (7)).[49] $^{\cdot}O_2^-$ can also be hydrolyzed into $^1O_2$ (eqn (8)). Finally, IBU is attacked by the generated active species, degraded to produce intermediate products, and ultimately converted into CO_2 and H_2O (eqn (9)). In summary, the superior catalytic performance originates from synergistic interactions among surface Co^{2+} sites, O_V, and O_L, enabling abundant ROS generation through these interconnected pathways.

$$Co^{2+} + HSO_5^- \rightarrow Co^{3+} + {}^{\cdot}SO_4^- + OH^- \quad (1)$$

$$^{\cdot}SO_4^- + H_2O \rightarrow SO_4^{2-} + {}^{\cdot}OH + H^+ \quad (2)$$

$$Co^{3+} + Cu^+ \rightarrow Co^{2+} + Cu^{2+} \quad (3)$$

$$Cu^{2+} + HSO_5^- \rightarrow Cu^+ + {}^{\cdot}SO_5^- + H^+ \quad (4)$$

$$HSO_5^{\cdot -} \rightarrow {}^{\cdot}SO_5^- + H^+ + e^- \quad (5)$$

$$e^- + O_2 \rightarrow {}^{\cdot}O_2^- \quad (6)$$

$$O_V/O_L + HSO_5^- \rightarrow SO_4^{2-} + {}^1O_2 + H^+ \quad (7)$$

$$2{}^{\cdot}O_2^- + 2H_2O \rightarrow {}^1O_2 + H_2O_2 + 2OH^- \quad (8)$$

$$^{\cdot}SO_4^-/{}^1O_2/{}^{\cdot}OH/{}^{\cdot}O_2^- + IBU \rightarrow \text{intermediates} \rightarrow CO_2 + H_2O \quad (9)$$

3.5 IBU possible degradation pathways

To elucidate the degradation mechanism and pathways of IBU, intermediate products generated during the LCCZ-3/PMS treatment were analyzed by LC-MS. Nine primary intermediates were identified as summarized. The proposed degradation routes based on these intermediates, revealing two principal pathways (Fig. 9). The major active species attack C position of IBU propionic acid group, followed by decarboxylation and hydroxylation to form intermediate P1 (m/z = 178),[50] which is subsequently demethylated and hydroxylated to yield P2 (m/z = 166). P2 then converts to P3 (m/z = 162) through dehydrogenative aldehyde formation. For pathway 2, oxygen substitution at IBU's carboxyl group generates P4 (m/z = 176),[51] which undergoes demethylation to form P5 (m/z = 148). P5 is further demethylated to P7 (m/z = 134), while parallel deisopropylation and carboxyl addition of P4 produces P6 (m/z = 164). These intermediates subsequently undergo aryl epoxidation to form P8 (m/z = 118) and P9 (m/z = 90). Zhang *et al.* degraded IBU by activating PS with Fe_3O_4 carbon composite materials,[52] and Choina *et al.* also found the same products in their study on IBU degradation.[53] The intermediates obtained after the IBU

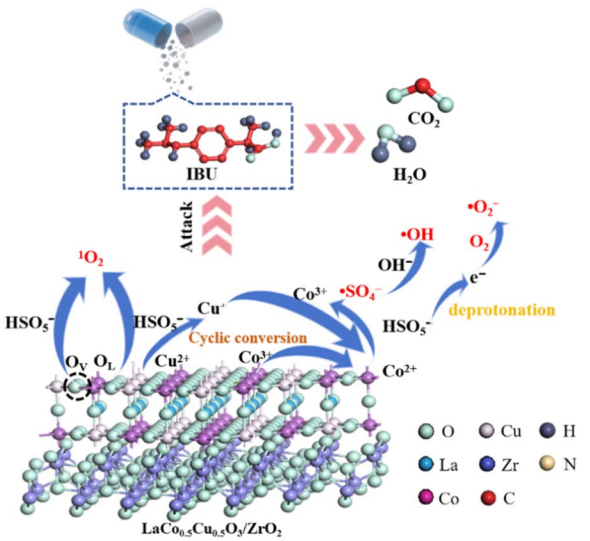

Fig. 8 Proposed catalytic mechanism for the activation of PMS by LCCZ.

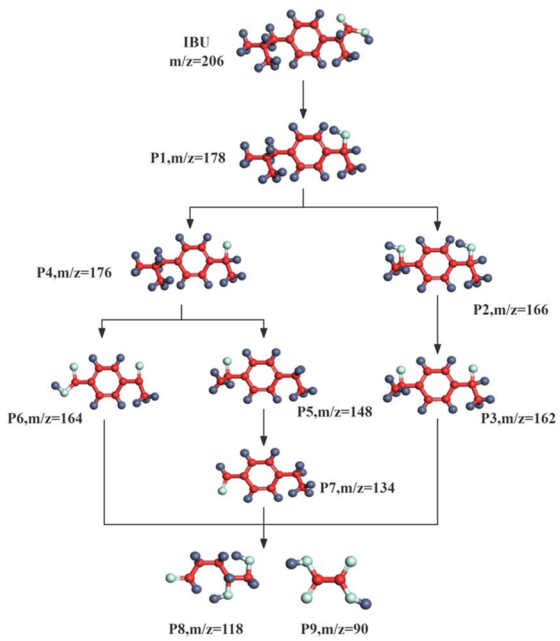

Fig. 9 IBU degradation pathway in LCCZ-3/PMS system.

reaction can continue to be oxidized by active substances to finally generate H_2O and CO_2, realizing the mineralization of IBU.

4 Conclusions

In this study, the sol–gel method was successfully employed to dope Cu into the B-site of $LaCoO_3$, and the resulting LaCoCu55 was successfully immobilized onto ZrO_2, and investigated LCCZ-3 as an efficient catalyst for PMS activation to degrade pollutants. Compared to previous Cu-doped $LaCoO_3$ systems, the ZrO_2-supported LCCZ-3 realizes the integration of structural stabilization, and electronic regulation *via* heterojunction formation, the introduction of Cu into $LaCoO_3$ promotes the redox cycle of Co^{2+}/Co^{3+}. After the reaction, the leaching concentration of Co ions in the 0.1 g L^{-1} catalyst was 0.522 mg L^{-1}, indicating no risk of secondary pollution. The LCCZ-3/PMS system exhibits superior practical applicability: it achieves 100% IBU removal at low catalyst/PMS dosages, maintains high activity in a wide pH/temperature range, and avoids secondary pollution, outperforming most reported heterogeneous catalysts. Under the action of $^1O_2$, $^{\cdot}SO_4^-$, $^{\cdot}OH$ and $^{\cdot}O_2^-$ generated by the material-catalyzed PMS, IBU undergoes oxidation to intermediate products including ketonic and alcoholic derivatives, ultimately mineralizing to CO_2 and H_2O *via* progressive oxidation. ZrO_2 introduces a unique nonradical pathway dominated by $^1O_2$ (derived from oxygen vacancies), which complements radical oxidation to improve the degradation efficiency and anti-interference ability, beyond the simple dispersion effect of traditional supports (*e.g.*, Al_2O_3, SiO_2). These results indicate that LCCZ-3 is a promising heterogeneous catalyst for activating peroxymonosulfate to degrade organic pollutants.

Author contributions

Zhaozhe Zhan: writing – original draft, data curation, visualization, validation. Xue Yu: formal analysis, supervision. Jun Wan: data curation, conceptualization. Xingchi Wang: investigation, data curation. Jibo Xiao: investigation, conceptualization. Yan Wu: writing – review & editing, funding acquisition. Zhiyong Yan: writing – review & editing, supervision.

Conflicts of interest

The authors declare that they have no known competing financial interests or personal relationships that could have appeared to influence the work reported in this paper.

Data availability

Data will be made available on request.

Acknowledgements

This work was financially supported by the Projects of the National Nature Science Foundation of China (No. 2257083011 and 22108069).

Notes and references

1 T. Olmez-Hanci and I. Arslan-Alaton, Comparison of sulfate and hydroxyl radical based advanced oxidation of phenol, *Chem. Eng. J.*, 2013, **224**(1), 10–16.
2 A. R. Ribeiro, O. C. Nunes, M. F. R. Pereira and A. M. Silva, An overview on the advanced oxidation processes applied for the treatment of water pollutants defined in the recently launched directive, *Environ. Int.*, 2015, **75**, 33–51.
3 B. Bouzayani, E. Rosales, M. Pazos and M. A. Sanromán, Homogeneous and heterogeneous peroxymonosulfate activation by transition metals for the degradation of industrial leather dye, *J. Cleaner Prod.*, 2019, **228**, 222–230.
4 Y. Liu, Y. Wang, Q. Wang and J. Zhang, Simultaneous removal of NO and SO_2 using vacuum ultraviolet light (VUV)/heat/peroxymonosulfate (PMS), *Chemosphere*, 2018, **190**, 431–441.
5 C. Cai, H. Zhang, X. Zhong and L. Hou, Ultrasound enhanced heterogeneous activation of peroxymonosulfate by a bimetallic FeCo/SBA-15 catalyst for the degradation of orange II in water, *J. Hazard. Mater.*, 2015, **283**(283), 70–79.
6 R. Xie, J. Ji, K. Guo, D. Lei, Q. Fan, D. Y. Leung and H. Huang, Wet scrubber coupled with UV/PMS process for efficient removal of gaseous VOCs: Roles of sulfate and hydroxyl radicals, *Chem. Eng. J.*, 2019, **356**, 632–640.
7 X. Liu, M. Chen and X. Zhang, Halogen anions (F^-, Cl^-, Br^-) modulated the localized microstructure of g-C_3N_4 to facilitate charge separation and transport and enhance photocatalytic activities, *Catal. Sci. Technol.*, 2024, **14**(14), 4036–4044.
8 X. Liu, X. Zhang and W. Chen, Pd nanoparticles supported on N-doped TiO_2 nanosheets: crystal facets, defective sites, and metal–support interactions boost reforming of formaldehyde solution for hydrogen production, *Langmuir*, 2022, **38**(44), 13532–13542.
9 S. Lu, G. Wang, S. Chen, H. Yu, F. Ye and X. Quan, Heterogeneous activation of peroxymonosulfate by $LaCo_{1-x}Cu_xO_3$ perovskites for degradation of organic pollutants, *J. Hazard. Mater.*, 2018, **353**, 401–409.
10 J. Xu, S. Gao, J. Xia, K. Zhang, Z. Shao, L. Wang and Y. Tian, Activatoin of peroxymonosulfate by Sr-doped $LaCo_{0.5}Cu_{0.5}O_3$ perovskite, *Chem. Ind. Eng. Prog.*, 2020, **39**(9), 3525.
11 F. Mahmoudi, S. Farhadi, P. Machek and M. Jarosova, Phosphotungstic acid supported on silica-coated $LaCoO_3$: Synthesis, characterization and application as a novel and efficient adsorbent for the removal of organic pollutants, *Polyhedron*, 2019, **158**, 423–431.
12 T. Yamaguchi, Application of ZrO_2 as a catalyst and a catalyst support, *Catal. Today*, 1994, **20**(2), 199–217.
13 H. Fujii, N. Mizuno and M. Misono, Pronounced Catalytic Activity of $La_{1-x}Sr_xCoO_3$ Highly Dispersed on ZrO_2 for

Complete Oxidation of Propane, *Chem. Lett.*, 1987, **16**(11), 2147–2150.

14 X. Liu, W. Chen, W. Wang, *et al.*, F-regulate the preparation of polyhedral $BiVO_4$ enclosed by High-Index facet and enhance its photocatalytic activity, *J. Colloid Interface Sci.*, 2022, **606**, 393–405.

15 Z. Li, D. Liao, G. Tian, *et al.*, Determination of Mn valence states in nanocatalysts during sustainable syngas conversion, *J. Am. Chem. Soc.*, 2025, **147**(36), 32548–32559.

16 R. B. Anjaneyulu, B. S. Mohan, G. P. Naidu and R. Muralikrishna, ZrO_2/Fe_2O_3/RGO nanocomposite: Good photocatalyst for dyes degradation, *Phys. E*, 2019, **108**, 105–111.

17 G. Tian, Z. Wang, C. Zhang, *et al.*, Nano Bifunctional Catalysts as Miniaturized Chemical Processes for CO_x-to-Aromatics Conversion, *Acc. Chem. Res.*, 2026, 508–519.

18 J. L. Sotelo, G. Ovejero, F. Martınez, J. A. Melero and A. Milieni, Catalytic wet peroxide oxidation of phenolic solutions over a $LaTi_{1-x}Cu_xO_3$ perovskite catalyst, *Appl. Catal., B*, 2004, **47**(4), 281–294.

19 K. Y. A. Lin, Y. C. Chen, T. Y. Lin and H. Yang, Lanthanum cobaltite perovskite supported on zirconia as an efficient heterogeneous catalyst for activating Oxone in water, *J. Colloid Interface Sci.*, 2017, **497**, 325–332.

20 M. J. Hu, C. W. Liu, L. X. Zhao, X. R. Wang, Y. P. Song and L. J. Heng, Heterojunction Bi_2O_3-TiO_2 Nanofiber as Cataluminescence Material for Detection of Toluene, *Chin. J. Inorg. Anal. Chem.*, 2022, **50**(7), 1103–1111.

21 P. Gao, X. Tian, W. Fu, Y. Wang, Y. Nie, C. Yang and Y. Deng, Copper in $LaMnO_3$ to promote peroxymonosulfate activation by regulating the reactive oxygen species in sulfamethoxazole degradation, *J. Hazard. Mater.*, 2021, **411**, 125163.

22 L. Zhang, L. Zhang, Y. Sun and B. Jiang, Porous ZrO_2 encapsulated perovskite composite oxide for organic pollutants removal: enhanced catalytic efficiency and suppressed metal leaching, *J. Colloid Interface Sci.*, 2021, **596**, 455–467.

23 W. Lou, L. Peng, R. He, Y. Liu and J. Qiao, CuBi electrocatalysts modulated to grow on derived copper foam for efficient CO_2-to-formate conversion, *J. Colloid Interface Sci.*, 2022, **606**, 994–1003.

24 L. Wu, X. Shi, H. Du, Q. An, Z. Li, H. Xu and H. Ran, Ce-doped $LaCoO_3$ film as a promising gas sensor for ethanol, *AIP Adv.*, 2021, **11**(5), 055305.

25 S. Phokha, S. Pinitsoontorn, S. Maensiri and S. Rujirawat, Structure, optical and magnetic properties of $LaFeO_3$ nanoparticles prepared by polymerized complex method, *J. Sol-Gel Sci. Technol.*, 2014, **71**, 333–341.

26 X. Duan, K. O'Donnell, H. Sun, Y. Wang and S. Wang, Sulfur and nitrogen co-doped graphene for metal-free catalytic oxidation reactions, *Small*, 2015, **11**(25), 3036–3044.

27 P. H. T. Ngamou, K. Kohse-Höinghaus and N. Bahlawane, CO and ethanol oxidation over $LaCoO_3$ planar model catalysts: Effect of the thickness, *Catal. Commun.*, 2011, **12**(14), 1344–1350.

28 J. Cao, L. Lai, B. Lai, G. Yao, X. Chen and L. Song, Degradation of tetracycline by peroxymonosulfate activated with zero-valent iron: performance, intermediates, toxicity and mechanism, *Chem. Eng. J.*, 2019, **364**, 45–56.

29 J. Wang and S. Wang, Effect of inorganic anions on the performance of advanced oxidation processes for degradation of organic contaminants, *Chem. Eng. J.*, 2021, **411**, 128392.

30 J. Ma, Y. Yang, X. Jiang, Z. Xie, X. Li, C. Chen and H. Chen, Impacts of inorganic anions and natural organic matter on thermally activated persulfate oxidation of BTEX in water, *Chemosphere*, 2018, **190**, 296–306.

31 S. Singh, T. Dosani, A. S. Karakoti, A. Kumar, S. Seal and W. T. Self, A phosphate-dependent shift in redox state of cerium oxide nanoparticles and its effects on catalytic properties, *Biomaterials*, 2011, **32**(28), 6745–6753.

32 S. Zhu, P. Xiao, X. Wang, Y. Liu, X. Yi and H. Zhou, Efficient peroxymonosulfate (PMS) activation by visible-light-driven formation of polymorphic amorphous manganese oxides, *J. Hazard. Mater.*, 2022, **427**, 127938.

33 C. Shen, Y. Wang and J. Fu, Urchin-like Co_3O_4 anchored on reduced graphene oxide with enhanced performance for peroxymonosulfate activation in ibuprofen degradation, *J. Environ. Manage.*, 2022, **307**, 114572.

34 C. Tan, Y. Huang, X. Lin, P. Li, L. Su and Q. Wang, Insights into ibuprofen degradation in boron-doped CuO/PMS systems: Role of Cu, kinetics, mechanisms and degradation pathways, *J. Water Process. Eng.*, 2025, **69**, 106711.

35 X. Fu, Q. Zeng, L. Song, Y. Wu, R. Wang and Q. Zeng, Insight into the performance and mechanism of N, O, S-codoped porous carbon based CO single-atom catalysts in organic oxidation through peroxymonosulfate activation, *Chem. Eng. J.*, 2024, **497**, 154668.

36 M. Naderi and R. D. C. Soltani, Hybrid of ZnFe layered double hydroxide/nano-scale carbon for activation of peroxymonosulfate to decompose ibuprofen: Thermodynamic and reaction pathways investigation, *Environ. Technol. Innovation*, 2021, **24**, 101951.

37 G. Zhang, Y. Ding, W. Nie and H. Tang, Efficient degradation of drug ibuprofen through catalytic activation of peroxymonosulfate by Fe_3C embedded on carbon, *J. Environ. Sci.*, 2019, **78**, 1–12.

38 C. Tan, Y. Cai, X. Lin, P. Li, X. Peng, R. Dai, L. Su and Q. Wang, Boosted peroxymonosulfate activation process mediated by boron embedded CuO catalyst: Enhanced performance and synergistic mechanism, *Appl. Surf. Sci.*, 2025, **679**, 161177.

39 G. Zhou, Y. Xu, X. Zhang, Y. Sun, C. Wang and P. Yu, Efficient activation of peroxymonosulfate by cobalt supported used resin based carbon ball catalyst for the degradation of ibuprofen, *Materials*, 2022, **15**(14), 5003.

40 M. Ding, H. Xu, A. Wang, C. Yao, A. Wang and L. Gao, Water recovery from wastewater by γFe_2O_3@ $Ti_3C_2T_x$ nanocomposites based on peroxymonosulfate activation, *Sep. Purif. Technol.*, 2023, **305**, 122466.

41 Y. Zhang, T. Yang, R. Li, X. Cao, Y. Kan, B. Wei and X. Sun, Efficient degradation of ibuprofen by Co/Fe@ CNFs catalyst in the presence of peroxymonosulfate and persulfate: Characterization, performance, and mechanism comparison, *J. Taiwan Inst. Chem. Eng.*, 2022, **131**, 104161.

42 W. Chen, X. Li, X. Wei, G. Liao, J. Wang and L. Li, Activation of peroxymonosulfate for degrading ibuprofen *via* single atom Cu anchored by carbon skeleton and chlorine atom: The radical and non-radical pathways, *Sci. Total Environ.*, 2023, **858**, 160097.

43 W. J. Xia, F. Liu, S. B. Hao, T. Y. Huang, Z. M. Wang and J. B. Chen, Degradation of OG with Peroxymonosulfate Activated by a $MnFe_2O_4$-graphene Hybrid, *Environ. Sci.*, 2018, **39**(5), 2202–2210.

44 O. Fónagy, E. Szabo-Bardos and O. Horváth, 1, 4-Benzoquinone and 1, 4-hydroquinone based determination of electron and superoxide radical formed in heterogeneous photocatalytic systems, *J. Photochem. Photobiol., A*, 2021, **407**, 113057.

45 E. Appiani, R. Ossola, D. E. Latch, P. R. Erickson and K. McNeill, Aqueous singlet oxygen reaction kinetics of furfuryl alcohol: effect of temperature, pH, and salt content, *Environ. Sci.: Processes Impacts*, 2017, **19**(4), 507–516.

46 Y. Wang, H. Sun, H. M. Ang, M. O. Tadé and S. Wang, 3D-hierarchically structured MnO_2 for catalytic oxidation of phenol solutions by activation of peroxymonosulfate: Structure dependence and mechanism, *Appl. Catal., B*, 2015, **164**, 159–167.

47 C. Chen, F. Li, H. L. Chen and M. G. Kong, Interaction between air plasma-produced aqueous $^1O_2$ and the spin trap DMPO in electron spin resonance, *Phys. Plasmas*, 2017, **24**(10), 4986008.

48 C. Liang, C. F. Huang, N. Mohanty and R. M. Kurakalva, A rapid spectrophotometric determination of persulfate anion in ISCO, *Chemosphere*, 2008, **73**(9), 1540–1543.

49 M. Hammad, S. Angel, A. K. Al-Kamal, A. Asghar, A. S. Amin, M. A. Kräenbring, H. T. A. Wiedemann, V. Vinayakumar, M. Y. Ali, P. Fortugno, C. Kim, T. C. Schmidt, C. W. M. Kay, C. Schulz, D. Segets and H. Wiggers, Synthesis of novel $LaCoO_3$/graphene catalysts as highly efficient peroxymonosulfate activator for the degradation of organic pollutants, *Chem. Eng. J.*, 2023, **454**, 139900.

50 Y. F. Rao, D. Xue, H. Pan, J. Feng and Y. Li, Degradation of ibuprofen by a synergistic UV/Fe (III)/oxone process, *Chem. Eng. J.*, 2016, **283**, 65–75.

51 M. Kwon, S. Kim, Y. Yoon, Y. Jung, T. M. Hwang, J. Lee and J. W. Kang, Comparative evaluation of ibuprofen removal by UV/H_2O_2 and UV/$S_2O_8^{2-}$ processes for wastewater treatment, *Chem. Eng. J.*, 2015, **269**, 379–390.

52 B. T. Zhang, Q. Wang, Y. Zhang, Y. Teng and M. Fan, Degradation of ibuprofen in the carbon dots/Fe_3O_4@carbon sphere pomegranate-like composites activated persulfate system, *Sep. Purif. Technol.*, 2020, **242**, 116820.

53 J. Choina, H. Kosslick, C. Fischer, G. U. Flechsig, L. Frunza and A. Schulz, Photocatalytic decomposition of pharmaceutical ibuprofen pollution in water over titania catalyst, *Appl. Catal., B*, 2013, **129**, 589–598.